How does the phytoplankton-light feedback affect the marine N_2O inventory?

Sarah Berthet [1*], Julien Jouanno [2], Roland Séférian [1], Marion Gehlen [3], William Llovel [4]

[1] CNRM, Université de Toulouse, Météo-France, CNRS, Toulouse, France
[2] LEGOS, Université de Toulouse, IRD, CNRS, CNES, UPS, Toulouse, France
[3] LSCE, Université Paris-Saclay, Institut Pierre Simon Laplace, Gif-Sur-Yvette, France
[4] LOPS, CNRS/University of Brest/IFREMER/IRD, Brest, France

([*]correspondence: sarah.berthet@meteo.fr)

Abstract

The phytoplankton-light feedback (PLF) describes the interaction between phytoplankton biomass and the downwelling shortwave radiation entering the ocean. The PLF allows to simulate differential heating across the ocean water column as a function of phytoplankton concentration. Only one third of the Earth system models contributing to the 6th phase of the Coupled Model Intercomparison Project (CMIP6) includes a complete representation of the PLF. In other models, the PLF is approximated either by a prescribed climatology of chlorophyll or not represented at all. Consequences of an incomplete representation of the PLF on the modelled biogeochemical state have not yet been fully assessed and remain a source of multi-model uncertainty in future projection. Here, we evaluate within a coherent modelling framework how representations of the PLF of varying complexity impact ocean physics and ultimately marine production of nitrous oxide (N_2O), a major greenhouse gas. We exploit global sensitivity simulations at 1-degree of horizontal resolution over the last two decades (1999-2018) coupling ocean, sea ice and marine biogeochemistry. The representation of the PLF impacts ocean heat uptake and temperature of the first 300 meters of the tropical ocean. Temperature anomalies due to an incomplete PLF representation drive perturbations of ocean stratification, dynamics and oxygen concentration. These perturbations translate into different projection pathways for N_2O production depending on the choice of the PLF representation. The oxygen concentration in the North Pacific oxygen minimum zone is overestimated in model runs with an incomplete representation of the PLF which results in an underestimation of local N_2O production. This leads to important regional differences of sea-to-air N_2O fluxes: fluxes are enhanced by up to 24% in the south Pacific and south Atlantic subtropical gyres, but reduced by up to 12% in oxygen minimum zones of the northern hemisphere. Our results based on a global ocean-biogeochemical model at CMIP6 state-of-the-art shed light on current uncertainties in modelled marine nitrous oxide budgets in climate models.

Plain language summary

Phytoplankton absorbs the solar radiation entering the ocean surface, and contributes to keep the associated energy in surface waters. This natural effect is either not represented in the ocean component of climate models, or in a simplified manner. We show that an incomplete representation of this biophysical interaction affects the way climate models simulate ocean warming, which leads to uncertainties in projections of oceanic emissions of an important greenhouse gas called the nitrous oxide.

Key-words: phytoplankton-light interaction; bio-physical feedback; nitrous oxide; N$_2$O; CMIP6 Earth system models; CNRM-ESM2-1; ocean-biogeochemical model; greenhouse gazes; marine emission; climate

Key points:
- forced ocean-biogeochemical simulations reveal that marine production of nitrous oxide is sensitive to the representation of the phytoplankton-light feedback
- the phytoplankton-light feedback perturbs the accumulation of heat and the ocean dynamics which drive changes in nitrous oxide production patterns
- an incomplete phytoplankton-light feedback overestimates sea-to-air N$_2$O fluxes by up to 24% in subtropical gyres and reduces them by up to 12% in oxygen minimum zones

1. Introduction

Feedbacks between the physical, biogeochemical, or ecosystem components of the ocean can trigger abrupt system changes (Heinze et al., 2021). At present the interactive phytoplankton-light feedback (PLF) is the only coupling in Earth system models between modelled marine biogeochemistry and ocean dynamics (Séférian et al., 2020). It implies that the chlorophyll (CHL) produced by the biogeochemical model is used to determine the fraction of shortwave radiation penetrating ocean surface waters. In this case, the CHL concentration profile used to approximate the influence of plankton biomass on the vertical redistribution of heat in the upper ocean is consistent with the one used to compute biogeochemical cycling.

a) Phytoplankton-light feedback (PLF)

Since the first observational evidence on how suspended matter in surface waters will impact light absorption by the ocean and change the radiative imbalance within the mixed layer (Kahru et al. 1993), this biophysical interaction has been gradually included to ocean models. Gildor and Naik (2005) highlighted the importance of considering monthly variations of CHL to capture the first-order effect of marine biota on light penetration in ocean models. Adding light-CHL interactions to numerical simulations affects oceanic processes over a wide range of spatial and temporal scales. Enabling a phytoplankton-light interaction modifies the hydrodynamics of the water column (Edwards et al., 2001; Edwards et al., 2004), the intensity of the spring-bloom in subpolar regions (Oschlies, 2004), the maintenance of the Pacific Cold Tongue (Anderson et al., 2007), the seasonality of the Arctic Ocean (Lengaigne et al., 2009), the strength of the tropical Pacific annual cycle, as well as the ENSO variability (Timmermann and Jin, 2002; Marzeion et al., 2005), the northward extension of the meridional overturning circulation (Patara et al., 2012) and the cooling of the Atlantic and Peru-Chili upwelling systems (Hernandez et al., 2017, Echevin et al., 2022).

However, the mean effect of the PLF on sea surface temperature has been argued to depend on the numerical framework (forced ocean versus coupled ocean-atmosphere models). The conflicting results reported in the literature were mainly due to diverging bio-optical protocols among models rather than to the inclusion of air-sea coupling. According to Park et al. (2014) atmosphere-ocean coupling amplifies the magnitude of PLF-induced changes, without altering the sign of the response obtained in ocean-only simulations. Two main causes were put forward

to explain the sign of the final heat perturbation: either an indirect dynamical response (Murtugudde et al., 2002; Löptien et al., 2009) or a direct thermal effect (Mignot et al., 2013; Hernandez et al., 2017). Hernandez et al. (2017) further distinguished a local from a remote thermal effect by highlighting the important role played by the advection of offshore CHL-induced cold anomalies in the Benguela upwelling waters. The interplay of these mechanisms is regionally variable (Park et al., 2014). Despite the diversity of modelled responses, a consensus emerges on the first order effect of PLF on the ocean physics, which is to perturb the ocean thermal structure (Nakamoto et al., 2001; Murtuggude et al., 2002; Oschlies, 2004; Manizza et al., 2005, 2008; Anderson et al., 2007; Lengaigne et al., 2007; Gnanadesikan and Anderson, 2009; Löptien et al., 2009; Patara et al., 2012; Mignot et al., 2013; Hernandez et al., 2017). By trapping more heat at the ocean surface in eutrophic regions, such as coastal or equatorial upwellings areas, the presence of phytoplankton initially increases the surface warming. Confining heat at the surface leads to less heat penetrating in subsurface. In some cases, the advection and upwelling of subsurface cold anomalies can lead to remote cooling effects (Hernandez et al., 2017; Echevin et al., 2022). Dynamical readjustment in response to perturbations in thermal structure has also been shown to have a cooling effect, by increasing upwelling of cold water to the ocean surface (Manizza et al. 2005; Marzeion et al., 2005; Nakamoto et al., 2001; Löptien et al., 2009; Lengaigne et al., 2007; Park et al., 2014). Because these effects depend on upper ocean stratification, an important role is attributed to modelled seasonal deepening of the mixed layer as it determines the intensity of the underlying temperature anomaly and its vertical movement to the surface. In other terms, whatever the temporality of the causal chain, changes in the PLF representation are expected to both perturb the ocean heat uptake, and trigger perturbations of both the water column stratification and associated ocean dynamics.

b) This study: implications for N_2O budget uncertainties

Nitrous oxide (N_2O) is a major ozone-depleting substance (Ravishankara et al., 2009; Freing et al., 2012) and a potent greenhouse gas, whose global warming potential is 265-298 times that of CO_2 for a 100-year timescale (Myhre et al., 2013). The spatial coherence between marine productive areas and observed hot-spots of N_2O production leads to question the impact of an incomplete representation of the PLF on the simulated N_2O inventory. Recent observational studies highlight that N_2O production is high in low-oxygen tropical regions and cold upwelling waters (Arévalo-Martinez et al. 2018; 2020; Yang et al., 2020; Wilson et al., 2020). N_2O becomes increasingly saturated in surface waters of equatorial upwelling regions due to the upward advection of N_2O-rich waters (Arévalo-Martínez et al., 2017). Regions known to account for the most productive areas of the ocean spatially coincide with highest N_2O production: 64% of the annual N_2O flux occurs in the tropics, and 20% in coastal upwelling systems that occupy less than 3% of the ocean area (Yang et al., 2020).

Despite recent advances, a large range of uncertainties still surrounds oceanic N_2O emissions as large areas of both the open and coastal ocean remain undersampled by observations (Wilson et al., 2020). In particular, the paucity of observational data over key source regions contributes to increase uncertainties. The recent global budget of Tian et al. (2020) estimates natural sources from soils and oceans to contribute with up to 57% to the total N_2O emissions between 2007 and 2016, with the ocean flux reaching 3.4 (2.5–4.3) Tg N yr^{-1}. A large uncertainty range is associated to the ocean flux estimate, as it is based on outputs from only a small

141 number of global ocean-biogeochemical models. Very few climate models, even in the current
142 CMIP6 generation, include emissions (and beforehand a complete representation of N cycling)
143 of N_2O fluxes: only 4 out of the 26 Earth system models considered in Séférian et al. (2020)
144 simulate marine N_2O emissions.

146 The last generation of Earth system models projects an enhanced ocean warming in response
147 to climate change, which is in turn expected to increase upper-ocean stratification (Sallée et
148 al., 2021) and to contribute to greater reductions in upper-ocean nitrate and subsurface oxygen
149 ventilation (Kwiatkowski et al., 2020). Ocean warming and deoxygenation constitute two
150 triggers of high-probability high-impact climate tipping points (Heinze et al., 2021) and are
151 identified as two of the main environmental factors influencing marine N_2O distributions (IPCC,
152 2019; Hutchins and Capone, 2022). Through its expected impacts on the upper ocean
153 stratification, the PLF representation could further change the oceanic N_2O source by
154 modulating the mixing between N_2O-rich water and intermediate depths, perturbing the way
155 N_2O-rich water reaches the air-sea interface (Freing et al., 2012).

157 Here we investigate how an incomplete representation of the PLF leads to uncertainties in N_2O
158 projection in an up-to-date global ocean-biogeochemical model making up the current
159 generation of Earth system models. Section 2 describes the numerical model and the set of
160 simulations, as well as the existing options to consider CHL modulations of the incoming
161 shortwave radiation. Section 3 presents the effect of an interactive PLF on the ocean heat
162 content, associated ocean stratification and dynamics, and its feedback on marine N_2O
163 inventory. Finally, Section 4 summarizes the main results, addresses their broader implications,
164 and discusses the future work motivated by this study.

166 **2. Methodology**

168 **a) Configuration of the global ocean-biogeochemical model**

170 Recent projections of future N_2O emissions contributing to intercomparison projects like CMIP6
171 are still based on Earth system models with a low spatial resolution (Séférian et al., 2020). For
172 sake of coherence with CMIP biogeochemical modelling efforts, in the following we use a global
173 ocean-biogeochemical configuration of the NEMO-PISCESv2 model (Madec, 2008; Aumont et
174 al., 2015) at 1° of horizontal resolution. This model corresponds to the oceanic component of
175 CNRM-ESM2-1 (Séférian et al., 2019) and is one of the few CMIP6-class models that contributed
176 to the Global N_2O budget (Tian et al., 2020). Our modelled ocean has 75 vertical levels and the
177 first level is at 0.5 meter depth. Vertical levels are unevenly spaced with 35 levels being in the
178 first 300 meters of depth. Atmospheric forcings of momentum, incoming radiation,
179 temperature, humidity, and freshwater are provided to the ocean surface by bulk formulae
180 following Large and Yeager (2009). Details on physical configuration are given in Berthet et al.
181 (2019). Using an ocean-only configuration allows to isolate the local response induced by the
182 PLF by not confounding it with potential inter-basin feedbacks acting through the atmosphere.

184 JRA55-do atmospheric reanalysis (Tsujino et al., 2018; Tsujino et al., 2020) provided the
185 atmospheric forcings of the ocean. The global domain was first spun-up under preindustrial
186 conditions during several hundred years ensuring that all fields approached a quasi-steady
187 state. The historical evolution of atmospheric CO_2 and N_2O concentrations was prescribed since

188   1850. To avoid the warming jump between the end of the spin-up and the onset of the
189   reanalyses in 1958, the first 5 years of JRA55-do forcings were cycled, followed by the complete
190   period of JRA55-do atmospheric forcing from 1958 to 2018.
191
192   **b) Experimental design: three representations of the PLF**
193
194   The control simulation (hereafter REF) together with the spin-up both account for a fully
195   interactive PLF: the penetration of shortwave radiation into the ocean surface is constrained
196   by the CHL concentration ([CHL]) produced by the PISCESv2 biogeochemical component (Figure
197   S1, REF).
198
199   PISCESv2 (Pelagic Interactions Scheme for Carbon and Ecosystem Studies v2) is a 3D
200   biogeochemical model which simulates the lower trophic levels of marine ecosystems
201   (nanophytoplankton, diatoms, microzooplankton and mesozooplankton), the biogeochemical
202   cycles of carbon and of the main nutrients (phosphate, nitrogen, iron, and silicate) along the
203   75 levels of our numerical ocean. A comprehensive presentation of the model is found in
204   Aumont et al. (2015). PISCESv2 simulates prognostic 3D distributions of nanophytoplankton
205   and diatom concentrations. The evolution of phytoplankton biomasses is the net outcome of
206   growth, mortality, aggregation and grazing by zooplankton. Growth rate of phytoplankton
207   mainly depends on the length of the day, depths of the mixed layer and of the euphotic zone,
208   the mean residence time of the cells within the unlit part of the mixed layer and includes a
209   generic temperature dependency (Eppley, 1972). Nanophytoplankton growth depends on the
210   external nutrient concentrations in nitrogen and phosphate (Monod-like parameterizations of
211   N and P limitations), and on Fe limitation which is modeled according to a classical quota
212   approach. The production terms for diatoms are defined as for nanophytoplankton, except that
213   the limitation terms also include silicate.
214
215   Light absorption by phytoplankton depends on the waveband and on the species (Bricaud et
216   al., 1995). A simplified formulation of light absorption by the ocean is used in our experiments
217   to calculate both the phytoplankton light limitation in PISCESv2 and the oceanic heating rate
218   (Lengaigne et al., 2007). In this formulation, visible light is split into three wavebands: blue
219   (400–500 nm), green (500–600 nm) and red (600–700 nm); for each waveband, the CHL-
220   dependent attenuation coefficients, k_R, k_G and k_B, are derived from the formulation proposed
221   in Morel and Maritorena (2001):
222

$$k_{WLB} = \sum_{\lambda_1}^{\lambda_2} \left(k(\lambda) + \chi(\lambda)[\text{CHL}]^{e(\lambda)} \right) \tag{1}$$

224   where WLB means the wavelength band associated to red (R), green (G) or blue (B), and
225   bounded by the wavelengths λ_1 and λ_2 as detailed above. $k(\lambda)$ is the attenuation coefficient
226   for optically pure sea water. $\chi(\lambda)$ and $e(\lambda)$ are fitted coefficients which allows to determine
227   the attenuation coefficients due to chlorophyll pigments in sea water (Morel and Maritorena,
228   2001).
229
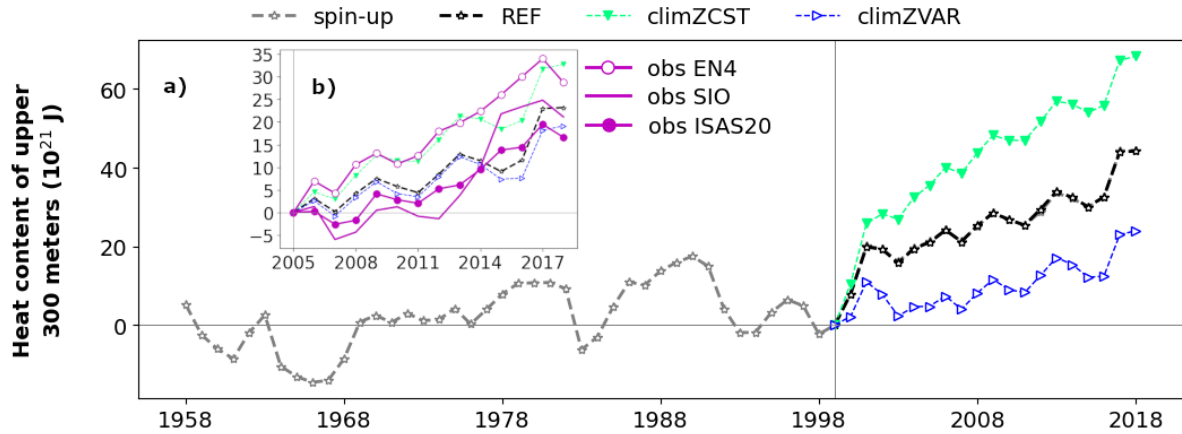
230
231 Figure 1: Modelled tropical [35°S-35°N] heat content of upper 300 m (OHC300; in ZJ) for each
232 simulation described in Table 1: REF (black; empty stars), climZCST (green; full downward
233 triangles) and climZVAR (blue; empty rightward triangles). In (a) final part of the spin-up has
234 been added in gray to illustrate the branching protocol in year 1999, and OHC300 anomalies
235 have been computed with respect to year 1999. Subplot (b) zooms over the Argo period to
236 compare modelled tropical OHC300 anomalies with 3 in situ-based products (see section 2c).
237
238 At year 1999 two sensitivity experiments were branched off (Figure 1). Both simulations
239 climZCST and climZVAR account for an incomplete and external PLF, as they consider an
240 observed climatology of surface [CHL] from ESACCI (Valente et al., 2016) in order to compute
241 the light penetration into sea water (Equation 1; Figure S1). These two simulations differ from
242 each other by the "realism" of the vertical profile derived in each grid point from the surface
243 value of the ESACCI CHL climatology to the level of light extinction (Table 1). climZCST uses
244 constant profiles of CHL spreading uniformly in the vertical direction (Figure 2, b and d-f).
245 climZVAR uses variable vertical profiles computed following Morel and Berthon (1989) (Figure
246 2, c and d-f). This set of simulations is representative of the several configurations used in the
247 case of CMIP intercomparison project.
248
249 Table 1: Experimental set-up.
250

Simulation	Which CHL fields to interact with incoming shortwave radiation?	PLF nature
REF	uses directly the 3D CHL produced by the biogeochemical component	interactive
climZCST	uses the prescribed monthly climatology of ESACCI CHL with a constant vertical profile, equal to the value of the surface climatology up to the level of light extinction	incomplete
climZVAR	uses the prescribed monthly climatology of ESACCI CHL with a variable vertical profile, derived from the surface climatology following Morel and Berthon (1989)	incomplete

251
252

253 In climZCST and climZVAR, PISCESv2 prognostically simulates [CHL], a key component of
254 biogeochemical cycles, but feedback of CHL on physics (stratification, ocean heat content) is
255 determined by the externally prescribed [CHL] climatology. The CHL concentrations used for
256 radiation or for biogeochemical cycles are not consistent, and phytoplankton biomass
257 computed by the biogeochemical model does not affect the physical properties of the ocean
258 waters.
259
260 Consequences on the marine biogeochemical mean state of incomplete representations of the
261 PLF are assessed in the following by difference to the control run REF. This methodology allows
262 to evaluate how different levels of realisms and complexity in resolving bio-physical interactions
263 impact the physical and biogeochemical content of the modelled ocean. A complete
264 description of the marine N_2O parameterization used in this model is presented in the
265 supplementary material.
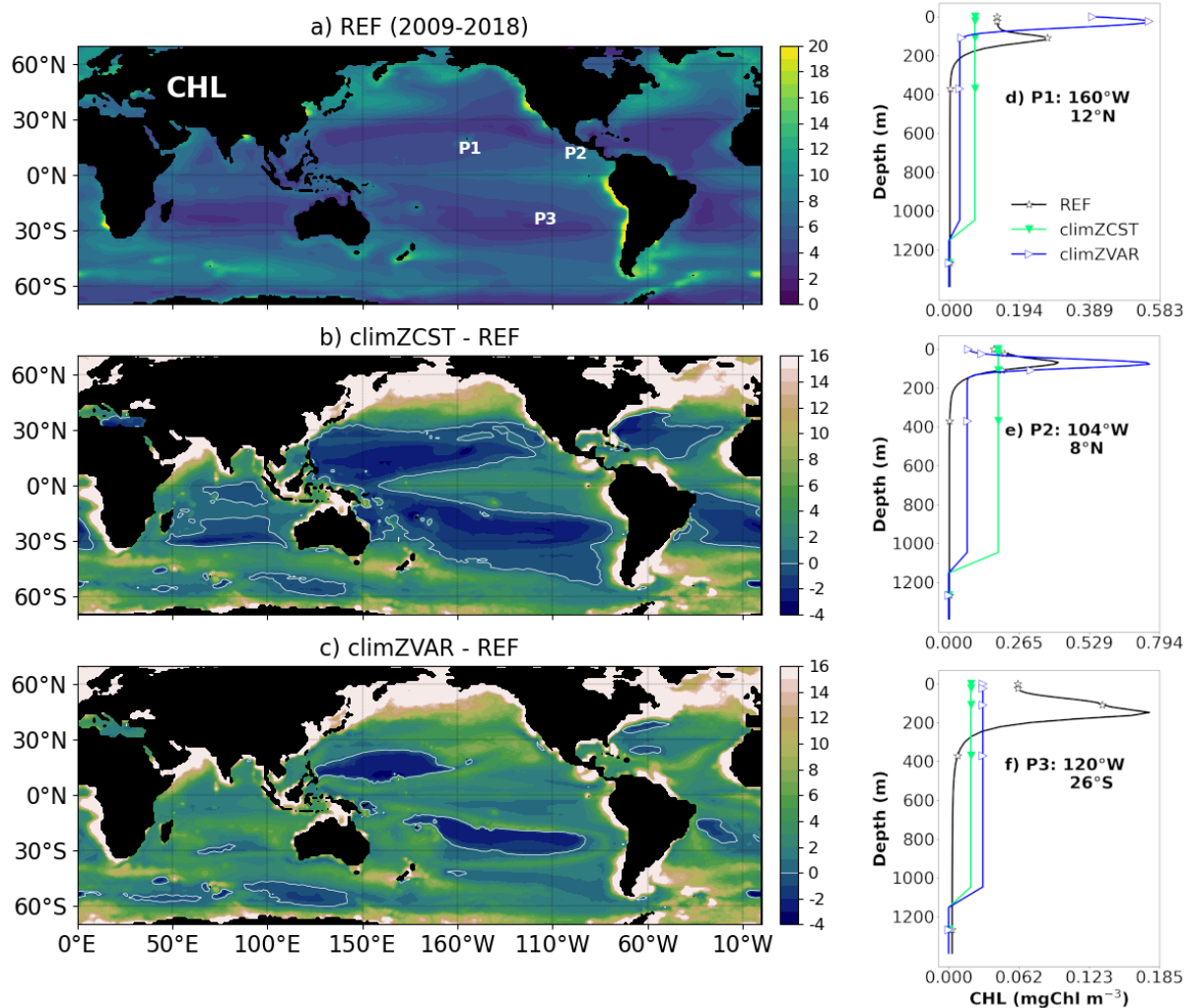
266
267 Figure 2: CHL concentration (mgCHL m^{-3}) interacting with the incoming shortwave radiation for
268 each numerical experiment (Table 1). Maps a-c) show annual means of the vertical sum over 0-
269 6000 m, a) as modelled over the 2009-2018 period for REF, and its differences with the external
270 CHL prescribed for b) climZCST and c) climZVAR experiments. Labels P1 to P3 on subplot a)
271 locate vertical profiles shown on subplots d-f).

272

273

274 c) Observations and analyses

275

276 Model results are compared with available observational-based gridded temperature and
277 salinity datasets. Ocean heat content (OHC) of the upper 0-300 meter layer was inferred from
278 three different products: i) the global objective analysis of subsurface temperature EN4 (Good
279 et al., 2013), ii) the SIO product of the Scripps Institution of Oceanography (Roemmich anf
280 Gilson, 2009), and iii) the ISAS20 optimal interpolation product released by Ifremer
281 (Kolodziejczyk et al., 2019; Kolodziejczyk et al., 2021). While the SIO and ISAS20 products
282 consider only Argo temperature and salinity profiles, the EN4 dataset considers all types of *in*
283 *situ* profiles providing temperature and salinity (when available). These three *in situ*-based
284 datasets are considered since 2005, the year the Argo coverage became sufficient to
285 characterize the global ocean. Details on OHC computation are given in Llovel and Terray (2016)
286 and Llovel et al. (2022). The authors also refer to cross-validations of OHC of deeper layers (0-
287 700 m and 0-2000 m) against OHC anomalies from World Ocean Atlas 2009 (Levitus et al.,
288 2012). A monthly climatology (1955-2012) of oceanic temperature from World Ocean Atlas
289 2013 version 2 (Locarnini et al., 2013) was used to evaluate modelled temperatures. Modelled
290 O_2 was compared to the annual climatology of O_2 from World Ocean Atlas 2013 (Garcia et al.,
291 2014) and modelled CHL was compared to the 3D monthly climatological global product
292 estimated from merged satellite and hydrological data of Uitz et al. (2006). Modelled N_2O
293 partial pressure difference across the air-sea interface (Dpn2o) was compared to the recent
294 dataset of Dpn2o observations compiled by Yang et al. (2020).

295

296 In the following temporal means cover the last 10 years of simulations, from 2009 to 2018. In
297 other analyses the whole simulated period is shown (1999-2018).

298

299 3. Results

300

301 a) Impact of PLF on the upper ocean heat content and dynamics

302

303 Meridional sections reveal that heat perturbations in response to changing CHL fields
304 interacting with light are limited to the top 0-300 m layer of the ocean and predominantly affect
305 the tropical area (Figure 3 and Figure S2, c-d).

306

307 The largest temperature anomalies are observed near the thermocline depth and reflect upper
308 ocean warming and deepening of the thermocline in climZCST (Figure 3c), and cooling and
309 shallowing of the thermocline in climZVAR (Figure 3d). In climZCST the ocean warming reflects
310 large-scale patterns of a tropical CHL deficit compared to REF (Figure 2, b). Temperature
311 differences are lower in the near-surface layer (0-50 m) than in the 50-300 m layer. This is
312 expected as a result from weak stratification but also from simulations run with a forced
313 atmosphere in which the temperature of the ocean surface layer is constrained by the
314 atmospheric prescribed state.

315

316 When using an incomplete representation of the PLF, two contrasting trends of the upper
317 ocean heat content (OHC) emerge compared to our control run REF (Figure 1a). Over the Argo
318 period (2005-present) EN4 estimates of tropical OHC300 are in very good agreement with our
319 warmest simulation climZCST (Figure 1b), while the two other dataproducts SIO and ISAS20 are

320 in better agreement with our control run REF and with climZVAR. The good accordance
321 between modeled OHC300 and observations is not a systematic feature of model-data
322 comparisons (Cheng et al., 2016; Liao et al., 2022). Moreover, non-negligible differences exist
323 among OHC dataproducts which are generally particularly strong in the upper 0-300 m layer
324 (Lyman et al., 2010; Liang et al., 2021). The spread between these products at the end of the
325 2005-2018 period (12.1 10^{21} J) is comparable to that of our numerical set (13.6 10^{21} J). The
326 modelled OHC in REF is in very good agreement with current global mean *in situ* observations
327 (Meyssignac et al., 2019; see their Figure 11) and with OHC anomalies derived from World
328 Ocean Atlas 2009 (Levitus et al., 2012). In accordance with these observations, our ocean-
329 biogeochemical model simulates a global mean increase of OHC over the 2006-2016 period of
330 order 40 10^{21} J for the upper 700 m, and of about 70 10^{21} J for the 0-2000 m layer.
331
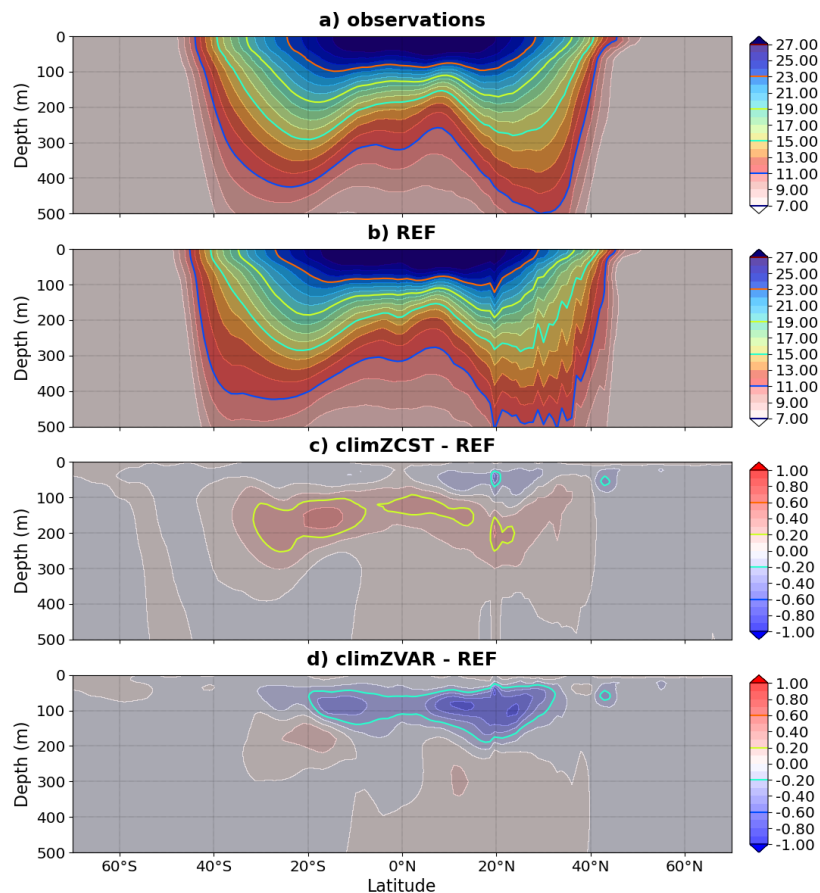
Figure 3: Mean 2009-2018 meridional section of temperature (°C) averaged over 0-360°E for
a) observations, b) REF and its differences with c) climZCST and d) climZVAR.

334 Subsurface thermal anomalies develop rapidly (Figure S3) after branching of climZVAR and
335 climZCST in 1999. The dipole structure of the anomaly seen in climZCST reflects the surface
336 heat trapping in REF and the associated subsurface cooling (Figure S3, b). Indeed in climZCST
337 the vertically constant and weaker concentrations of CHL trap less incoming shortwave than
338 the CHL maximum seen in REF between 0 and 100 m depth (Figure 2, d-f). The negative anomaly
339 in climZVAR suggests that the parameterization of Morel and Berthon (1989) contributes to
340 underestimate the ocean heat uptake (Figure S3, c and Figure S2, d) compared to REF. This heat
341 deficit results from the overestimation of the vertical integral of CHL over large areas of the

342 tropical domain in climZVAR compared to REF (Figure 2, c). As a result, the energy associated
343 with the incoming radiation is caught in surface waters without being distributed over the water
344 column.
345
346 In both climZCST and climZVAR the subsurface temperature anomaly deepens progressively
347 over the first six years of simulation as a result of vertical mixing (Figure S3). This evolution
348 indicates that part of the OHC300 differences between simulations comes from the adjustment
349 of climZCST and climZVAR to the spin-up mean state yielded by an interactive PLF. It can be
350 expected that experiments having spin-ups run with different representations of the PLF, would
351 give even stronger sensitivities than those highlighted in this study. The sensitivities of OHC300
352 to the PLF formulation evaluated here should be considered at the lower end of estimate of
353 OHC discrepancies that may emerge from changing the PLF representation.
354
355 Prescribing a constant vertical profile of CHL (climZCST) to compute the penetration of the
356 radiation into the ocean increases the OHC300 by more than 20 10^{21} J during the last two
357 decades (1999-2018) compared to REF (Figure 1). This rise of OHC300 decreases the vertically-
358 integrated tropical potential density of the upper 300 m at the end of the simulated period by
359 5 kg/m^2 compared to REF (Figure S4). The opposite trend (a reduced OHC300 compared to REF)
360 is simulated with the same state-of-the-art CMIP6 ocean-biogeochemical model when
361 considering a variable vertical profile of CHL (climZVAR). However Figure 1 highlights that the
362 simulation using a consistent CHL for interacting with both incoming shortwave radiation and
363 biogeochemical cyclings (REF) does not amplify one of these two trends, as climZCST and
364 climZVAR surround REF. Average ranges of uncertainties associated with the PLF
365 representation over the extended tropical domain (35°S-35°N) exceed 40 10^{21} J in terms of
366 OHC300 (Figure 1), 4 meters for the thermocline depth and more than 9 kg/m^2 for the
367 vertically-integrated potential density perturbation (Figure S4).
368
369 Similar to OHC300, ranges of uncertainty for the OHC estimates of deeper layers (0-700 m and
370 0-2000 m) also slightly exceed 40 10^{21} J. Such uncertainty ranges are quite important as they
371 are obtained by only changing the PLF representation in a single ocean-biogeochemical model.
372 By comparison and in the context of OMIP protocols, Tsujino et al. (2020) give spreads between
373 CMIP model estimates of the order of 50 10^{21} J for the OHC of the upper 700m after 20 years
374 (please refer to their Figure 24, a-b). Regarding the OHC integrated over the 0-2000m layer,
375 they report an inter-model spread between 50 and 100 10^{21} J, depending on the OMIP protocol
376 considered (see their Figure 24, d-e). The OHC300 uncertainty of 40 10^{21} J triggered by the
377 representation of the PLF in our set of simulations has a comparable order of magnitude than
378 the current spread of multi-model estimations of OHC. The present study suggests that part of
379 the OHC multi-model uncertainty in current climate models may be due to different
380 representations of the phytoplankton-light interaction.
381
382 The heat and associated density perturbations also cause dynamical modifications of upper
383 ocean currents (Figure 4). Absolute differences in upper ocean velocities (average between 0
384 and 300m depth) are between |0.05| and |0.6| cm/s with strongest differences along the
385 equator revealing perturbations of the equatorial undercurrent (Figure 4, b and c). Circulation
386 around the subtropical gyres is also impacted, in particular for the South Pacific subtropical
387 gyre. These modifications of zonal and meridional dynamics spread over the entire tropical
388 latitudes, from 30°S to 30°N, strongly supporting the idea that heat perturbations induced by

different interactions between CHL and incoming shortwave cause non-negligible modifications of the equatorial and tropical ocean dynamics.
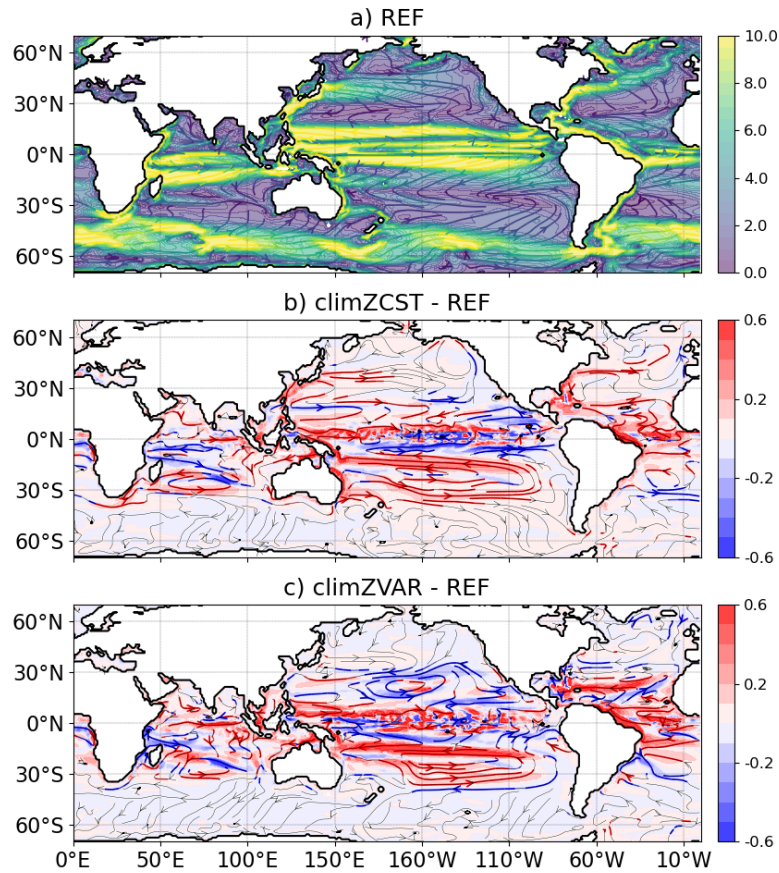
Figure 4: Annual mean speed (color; cm/s) and streamlines of oceanic currents between 0-300 m over the 2009-2018 period for a) REF, and its differences with b) climZCST and c) climZVAR. In b-c) streamlines are colored when absolute speed are larger than 0.05 cm/s.

b) PLF impact on N_2O production

Perturbations of the annual pycnocline depth (Figure 5, a-c) highlight a vertical adjustment to the heat (Figure S2) and subsequent large-scale dynamical anomalies (Figure 4). Variations of the pycnocline integrate perturbations of both thermal and salinity stratifications. However, in our simulations heat anomalies appear to drive perturbations and pycnocline depth anomalies mainly reflect those of the thermocline. The cold anomaly dominating the tropical domain in climZVAR (Figure S2, d) appears to be vertically redistributed, as it triggers an upward displacement of the isopycnals (Figure 5, c). In contrast to the anomalies seen over most of the tropical Pacific, a deepening of the isopycnals reaching up to 20 meters is modelled in both South Pacific and Atlantic subtropical gyres in climZCST and climZVAR (Figure 5, b and c). Over these subtropical gyres heat is redistributed along the vertical as the subsurface warm anomaly dives. The subduction of these heat anomalies causes in turn a deepening of the pycnocline (Figure 5, b and c). As stressed by Sweeney et al. (2005), small changes in CHL concentration (Figure S5) may have important effects on the mixed layer depth in these subtropical gyres due to low local wind speeds and low mixing conditions. This is thought to explain the large sensitivity we observe in terms of pycnocline depth (Figure 5) and ocean heat content in these

regions. In line with their results, our set of simulations highlights that small CHL changes in low productivity regions trigger a vertical redistribution of density anomalies affecting the stratification.
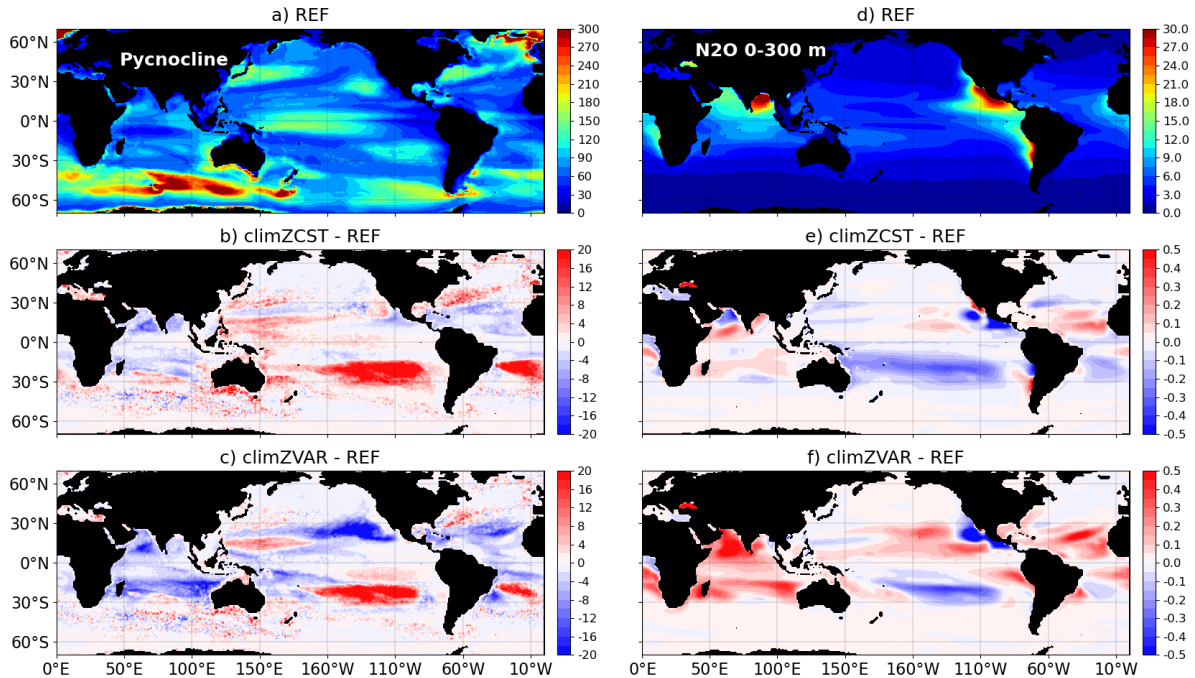
Figure 5: a-c) Depth of annual pycnocline (m) for 2009-2018 computed as the annual mean depth of the maximum of the Brunt-Väisälä frequency $N^2(T, S)$ over the water column (Maes and O Kane, 2014). d-f) Mean $[N_2O]$ (μmolN/m^3) over the first 300 meters depth. For REF (upper panel) and its mean-state differences with climZCST (middle panel) and climZVAR (bottom panel).

Anomalies of N_2O concentration integrated over the first 300 meters of the water column (Figure 5, e and f) are in good agreement with patterns of pycnocline anomalies over the tropics (Figure 5, b and c). These comparable spatial structures attest that N_2O anomalies are driven by perturbations of stratification in large parts of the tropical domain.

In the South Pacific subtropical gyre, the concomitance of i) an increased temperature (Figure S2, c and d), ii) a reinforced transport (Figure 4, b and c) and iii) a weakened stratification illustrated by a local deepening of the pycnocline (Figure 5, b and c), contributes to decrease the N_2O concentration in both climZCST and climZVAR (Figure 5, e and f). In contrast, in the South Indian Ocean and North tropical Atlantic the increase of N_2O concentration seems to be mainly driven by the mean shoaling of the local pycnocline, as both regions exhibit contrasted perturbations in terms of transport and temperature. Finally, in the North Pacific oxygen minimum zone, the strong N_2O deficits in both climZCST and climZVAR compared to REF do not respond to stratification and transport anomalies but are rather driven by a local rise of O_2 concentration (Figure S6). Considering an incomplete PLF contributes to overestimate the oxygen concentration in this oxygen minimum zone and leads to a lack of local N_2O production.

The relationship between N_2O concentration and OHC300 in the Tropical Ocean is derived from a linear regression for each of the three 20-years simulations (Figure 6). The resulting slopes

445   allow to identify three distinct tropical N₂O production pathways along time as a function of
446   the oceanic heat uptake: from 0.3 μmolN m⁻² per ZJ for the most simplified PLF scenario
447   climZCST, to 1 μmolN m⁻² per ZJ for climZVAR. The slope of the simulation with the higher level
448   of realism in terms of interactivity (REF) appears a solution between the two previous extremes,
449   as it increases its N₂O production by 0.8 μmolN m⁻² per ZJ. Each of these N₂O production
450   pathways will translate into a different temporal evolution of the N₂O budget and hence future
451   climate. This result stresses the importance of having an interactive PLF in order to neither
452   overestimate nor underestimate the N₂O production projections due to a simplified
453   representation of the PLF.
454
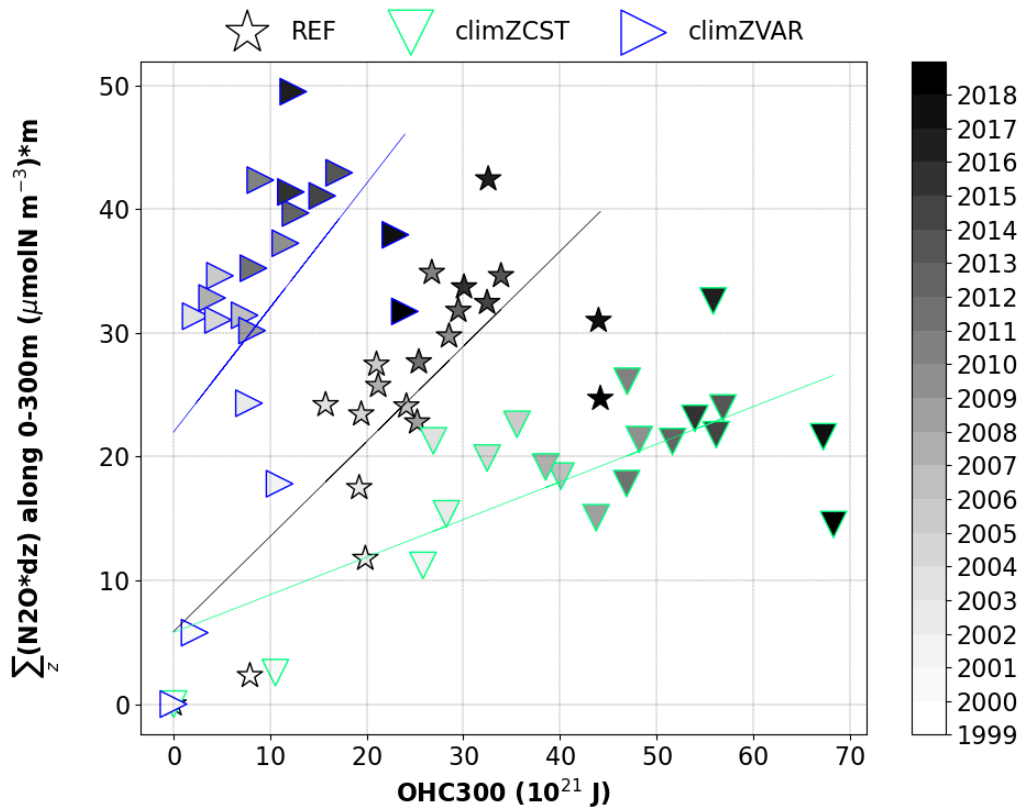
455
456   Figure 6: Annual N₂O inventory vertically integrated over the first 300 meters depth
457   (μmolN/m²) as a function of the annual OHC300 (ZJ) and averaged over an extended tropical
458   domain (35°S-35°N). All points reflect anomalies compared to year 1999.

459
460   c) Impacts on oceanic N₂O emissions
461
462   By perturbing the OHC, the ocean dynamics and the N₂O production, the way PLF is modelled
463   has non-negligible consequences on Dpn2o and thus on N₂O emissions at the air-sea interface
464   (Figure 7). Because the atmospheric partial pressure of N₂O is identical among simulations,
465   differences in Dpn2o are driven by changes in surface oceanic N₂O concentration normalized
466   by those in N₂O solubility. Since solubility is mainly driven by temperature and because surface
467   temperature anomalies are very weak (Figure S3, c and d), we do not expect solubility
468   perturbations close to the surface. It results that spatial patterns of Dpn2o anomalies (Figure
469   7) reflect differences in surface oceanic N₂O concentration.
470

471 Compared to a scenario considering a fully interactive PLF (REF), an incomplete representation
472 of the PLF underestimates Dpn2o in all oxygen minimum zones of the northern hemisphere,
473 which are strong emission zones (Figure 7, c and d). Large Dpn2o anomalies of -2.5 natm
474 encompasses northern parts of the oxygen minimum zones of the Indian, Pacific and Atlantic
475 oceans and anomalies reach up to -5 natm locally. Consequently, climZCST and climZVAR
476 underestimate N_2O fluxes by more than 12% in these oxygen minimum regions compared to
477 REF. This result highlights that the representation of the PLF can be an important source of
478 uncertainty in modelling N_2O fluxes. As a matter of fact, the oceanic contribution to the recent
479 global N_2O budget by Tian et al. (2020) is based on only five global ocean-biogeochemical
480 models (as still only few models simulate marine N_2O emissions). These models have different
481 configurations of the PLF which adds considerable uncertainty to simulated marine N_2O
482 emissions.
483
484 In subtropical gyres, the strong and direct effect of temperature (Figure S2, c and d) on in-depth
485 N_2O concentration (Figure 5, e and f) is in line with Yang et al. (2020) who demonstrate that the
486 seasonality of Dpn2o in that regions is driven by a solubility regime. Both climZCST and
487 climZVAR overestimate Dpn2o in subtropical gyres of the South Pacific and South Atlantic
488 (Figure 7, c and d). This leads to an overestimation of the regional N_2O fluxes by 24% compared
489 to a simulation having a complete and interactive PLF representation (REF).
490
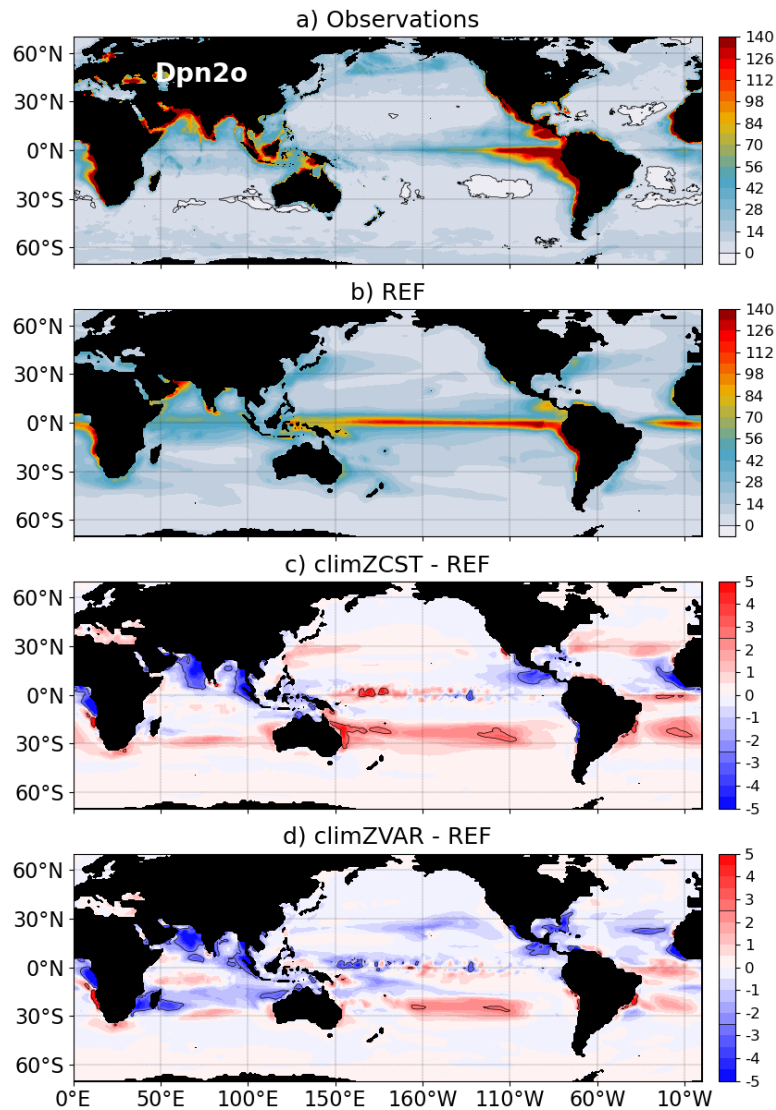
Figure 7: Mean sea-to-air Dpn2o (natm) computed from a) observations, b) REF over the 2009-2018 period, and its differences with c) climZCST and d) climZVAR compared to REF.

4. Discussion and conclusion

In this study we use the ocean component (including ocean physics, sea ice and marine biogeochemistry) of the global Earth system model CNRM-ESM2-1 which contributed to the last phase of the Coupled Model Intercomparison Project (CMIP6). Our ocean-biogeochemical model is one of the few currently able to represent an interactive phytoplankton-light feedback (PLF) by constraining the penetration of shortwave radiation into the ocean as a function of the CHL concentration produced by the biogeochemical model. Three simulations have been run at the horizontal resolution currently used for intercomparisons of Earth system models (1°). Analyses are based on differences between a control run with an interactive PLF (REF) and two experiments with an incomplete PLF (climZCST and climZVAR) using a prescribed CHL climatology to interact with the incoming solar radiation. Changing the approach to compute how CHL filters the light penetrating into the ocean highlights the consequences of using an interactive PLF.

510 Our results demonstrate that the approach commonly used to account for the impact of the
511 phytoplankton on light penetration significantly interfers with upper ocean heat uptake (Figure
512 1), the associated dynamics (Figure 4) and stratification in the tropics (Figure 5, a-c). Our set of
513 forced ocean-biogeochemical simulations reveals that marine production of nitrous oxide
514 (N_2O) is sensitive to the representation of the PLF (Figure 5, d-f). The heat perturbations add to
515 the uncertainty of modelled oceanic N_2O production and result in three N_2O production
516 trajectories along time (Figure 6) that in turn trigger regional differences of Dpn2o and sea-air
517 N_2O fluxes (Figure 7). Compared to an ocean model using a fully interactive PLF (REF), an
518 incomplete PLF results in an overestimation of N_2O fluxes by up to 24% in the South Pacific and
519 South Atlantic subtropical gyres, and a reduction by up to 12% in oxygen minimum zones of the
520 northern hemisphere. Our results based on a model at CMIP6 state-of-the-art emphasize an
521 overlooked important source of uncertainty in climate projections of marine N_2O production
522 and in current estimations of the marine nitrous oxide budget.

524 In subtropical gyres of the southern Hemisphere which are regions of low productivity, small
525 CHL changes have a strong and direct effect on temperature (Figure S2, c and d), transport
526 (Figure 4, b and c) and local stratification (Figure 5, b and c). These concomittant effects result
527 in a local decrease of N_2O concentrations in both experiments with a simplified PLF
528 representation (climZCST and climZVAR).

530 In forced ocean simulations, atmospheric forcings constrain surface temperature, salinity and
531 thus solubility. However, the N_2O concentration integrated over the upper 300 meters depth
532 of the water column (Figure 5, e-f) showed differences with the control run that follow those
533 of the in-depth temperature (Figure S2, c-d): in climZCST (climZVAR), a warmer (colder) tropical
534 ocean leads to a decreased (an increased) N_2O concentration. Because higher marine
535 greenhouse gas emissions will increase the temperature of the coupled atmosphere-ocean
536 system, adding an interactive atmospheric component is expected to amplify the PLF-induced
537 mean changes in marine N_2O concentration highlighted in this ocean-only numerical set (Park
538 et al., 2014; Asselot et al., 2022).

540 Our results also question the reliability of current modelled estimates of the area and volume
541 of oxygen minimum zones, as well as their trends in a future climate. The expansion rate of O_2-
542 depleted waters still remains unclear and its controlling mechanisms are not yet fully
543 understood and represented in today's models. Observation based assessments suggested that
544 the ocean has already lost around 2% of the global marine oxygen since 1960 (Schmidtko et al.,
545 2017). The expansion of oxygen minimum zones is expected to result in an increase of the
546 volume of suboxic water and to have an impact on the production and decomposition of N_2O
547 (Freing et al., 2012). Our set of simulations highlights that an incomplete representation of the
548 PLF underestimates the expansion of oxygen-depleted waters over the 20 years of simulation
549 in comparison to REF. In climZCST and climZVAR the global volume (0-1000 m) of hypoxic water
550 with [O_2] under 50 mmol m^{-3} is up to $2.3 \ 10^{14} \ m^3$ lower in 2018 compared to that of the control
551 run REF. Thus an incomplete representation of the PLF might lead to an underestimation by 1.2
552 % of the modelled tropical volume of low-oxygenated waters after 20 years.

554 Recent regional studies demonstrated that the interactive PLF strongly affects upwelling
555 systems of the South Pacific and Atlantic oceans (Hernandez et al., 2017; Echevin et al., 2021).
556 Coastal upwellings are known to be sites of high N_2O production with an annual N_2O flux

amounting to approximately 20% of the global fluxes while these systems occupy less than 3% of the ocean area (Yang et al., 2020). However, in the present study main modelled perturbations are rather localized over oxygen minimum zones or subtropical gyres (Figure 5; Figure 7). While the latter regional studies were performed at horizontal resolutions compatible with the complex dynamics of coastal upwellings (from 10 km to about 28 km), the resolution of climate models (~1-degree of horizontal resolution) does not allow to resolve these dynamics. A step further would be to evaluate how the sensitivity of N_2O emission to the representation of the PLF depends on the horizontal resolution by running simulations at higher resolution with the same climate model. This would help to better determine how coastal upwelling systems may impact the modelled N_2O inventory through different PLF representations, as well as the associated modelled range of uncertainty.

Code availability

Sources for NEMO and PISCESv2 codes are available from https://forge.nemo-ocean.eu/nemo.

Acknowledgements

The OHC data were collected and made freely available by the International Argo Program and the national programs that contribute to it (https://argo.ucsd.edu, https://www.ocean-ops.org). The Argo Program is part of the Global Ocean Observing System. R. Séférian acknowledges the European Union's Horizon 2020 research and innovation program under grant agreement No. 101003536 (ESM2025 − Earth System Models for the Future).

References

Anderson,W. G., A. Gnanadesikan, R. Hallberg, J. Dunne, and B. L. Samuels (2007), Impact of ocean color on the maintenance of the Pacific Cold Tongue, Geophys. Res. Lett., 34, L11609, doi:10.1029/2007GL030100.

Asselot, R., Lunkeit, F., Holden, P. B., & Hense, I. (2022). Climate pathways behind phytoplankton-induced atmospheric warming. Biogeosciences, 19(1), 223-239.

Aumont, O., Ethé, C., Tagliabue, A., Bopp, L., & Gehlen, M. (2015). PISCES-v2: An ocean biogeochemical model for carbon and ecosystem studies. Geoscientific Model Development, 8, 2465–2513.

Arévalo-Martinez, D. L., A. Kock, T. Steinhoff, P. Brandt, M. Dengler, T. Fischer, A. Körtzinger, and H. W. Bange (2017), Nitrous oxide during the onset of the Atlantic cold tongue, J. Geophys. Res. Oceans, 122, 171–184, doi:10.1002/2016JC012238

Arévalo-Martínez, D. L., Steinhoff, T., Brandt, P., Körtzinger, A., Lamont, T., Rehder, G., & Bange, H. W. (2019). N2O emissions from the northern Benguela upwelling system. Geophysical Research Letters, 46, 3317–3326. https://doi.org/10.1029/2018GL081648

Berthet, S., Séférian, R., Bricaud, C., Chevallier, M., Voldoire, A., & Ethé, C. (2019). Evaluation of an online grid-coarsening algorithm in a global eddy-admitting ocean biogeochemical model. Journal of Advances in Modeling Earth Systems, 11, 1759–1783. https://doi.org/10.1029/2019MS001644

Bopp, L., Resplandy, L., Orr, J. C., Doney, S. C., Dunne, J. P., Gehlen, M., Halloran, P., Heinze, C., Ilyina, T., Séférian, R., Tjiputra, J., and Vichi, M. (2013). Multiple stressors of ocean ecosystems in the 21st century: projections with CMIP5 models, Biogeosciences, 10, 6225–6245, doi:10.5194/bg-10-6225-2013.

607

608 **Bricaud**, A., Babin, M., Morel, A., and Claustre, H.: Variability in the chlorophyll-specific absorption
609 coefficients of natural phytoplankton: analysis and parameterization, J. Geophys. Res., 100, 13321–13332,
610 1995.

611

612 **Cheng**, L., Trenberth, K. E., Palmer, M. D., Zhu, J., and Abraham, J. P.: Observed and simulated full-depth
613 ocean heat-content changes for 1970–2005, Ocean Sci., 12, 925–935, https://doi.org/10.5194/os-12-925-
614 2016, 2016.

615

616 **Cocco**, V., Joos, F., Steinacher, M., Frölicher, T. L., Bopp, L., Dunne, J., Gehlen, M., Heinze, C., Orr, J.,
617 Oschlies, A., Schneider, B., Segschneider, J., and Tjiputra, J. (2013). Oxygen and indicators of stress for
618 marine life in multi-model global warming projections, Biogeosciences, 10, 1849–1868, doi:10.5194/bg-10-
619 1849-2013.

620

621 **Echevin**, V., Hauschildt, J., Colas, F., Thomsen, S., & Aumont, O. (2021). Impact of chlorophyll shading on
622 the Peruvian upwelling system. Geophysical Research Letters, 48, e2021GL094429.
623 https://doi.org/10.1029/2021GL094429

624

625 **Edwards**, A. M., Wright, D. G., Platt, T. (2004) Biological heating effect of a band of phytoplankton. *Journal*
626 *of Marine Systems*, 49, 89-103. doi: 10.1016/j.jmarsys.2003.05.011.

627

628 **Edwards**, A. M., Platt, T., Wright, D. G. (2001) Biologically induced circulation at fronts. *Journal of*
629 *geophysical research*, 49, 89-103. doi: 10.1016/j.jmarsys.2003.05.011.

630

631 **Eppley**, R. W.: Temperature and phytoplankton growth in the sea, Fish. Bull., 70, 1063–1085, 1972.

632

633 **Freing**, A., D. W. R. Wallace, and H. W. Bange, 2012: Global oceanic production of nitrous oxide. Philos. Trans.
634 R. Soc. London Ser. B, **367**, 1245–1255.

635

636 **Garcia**, H. E., R. A. Locarnini, T. P. Boyer, J. I. Antonov, O.K. Baranova, M.M. Zweng, J.R. Reagan, D.R.
637 Johnson, (2014). World Ocean Atlas 2013, Volume 3: Dissolved Oxygen, Apparent Oxygen Utilization, and
638 Oxygen Saturation. S. Levitus, Ed., A. Mishonov Technical Ed.; NOAA Atlas NESDIS 75, 27 pp.

639

640 **Gildor**, H., and N. H. Naik (2005), Evaluating the effect of interannual variations of surface chlorophyll on
641 upper ocean temperature, J. Geophys. Res., 110, C07012, doi:10.1029/2004JC002779.

642

643 **Gnanadesikan**, A., and W. G. Anderson (2009), Ocean water clarity and the ocean general circulation in a
644 coupled climate model, J. Phys. Ocean., 39, 314–332.

645

646 **Good**, S. A., M. J. Martin and N. A. Rayner, (2013). EN4: quality controlled ocean temperature and salinity
647 profiles and monthly objective analyses with uncertainty estimates, Journal of Geophysical Research:
648 Oceans, doi:10.1002/2013JC009067

649

650 **Hajima**, T., Watanabe, M., Yamamoto, A., Tatebe, H., Noguchi, M. A., Abe, M., Ohgaito, R., Ito, A., Yamazaki,
651 D., Okajima, H., Ito, A., Takata, K., Ogochi, K., Watanabe, S., and Kawamiya, M. (2020). Development of the
652 MIROC-ES2L Earth system model and the evaluation of biogeochemical processes and feedbacks, Geosci.
653 Model Dev., 13, 2197–2244, https://doi.org/10.5194/gmd-13-2197-2020.

654

655 **Heinze**, C., T. Blenckner, H. Martins, D. Rusiecka, R. Döscher, M. Gehlen, N. Gruber, E. Holland, Ø. Hov, F.
656 Joos, J. B. R. Matthews, R. Rødven and S. Wilson (2021). The quiet crossing of ocean tipping points,
657 Proceedings of the National Academy of Sciences, 118 (9) e2008478118; DOI: 10.1073/pnas.2008478118

658

659 **Hernandez**, O., J. Jouanno, V. Echevin, and O. Aumont (2017), Modification of sea surface temperature by
660 chlorophyll concentration in the Atlantic upwelling systems, J. Geophys. Res. Oceans, 122, 5367–5389,
661 doi:10.1002/2016JC012330.
662
663 **Hutchins**, D.A., Capone, D.G. The marine nitrogen cycle: new developments and global change. Nat Rev
664 Microbiol (2022). https://doi-org.insu.bib.cnrs.fr/10.1038/s41579-022-00687-z
665
666 **Ilyina**, T., K. D. Six, J. Segschneider, E. Maier-Reimer, H. Li, and I. Núñez-Riboni (2013), Global ocean
667 biogeochemistrymodel HAMOCC: Model architecture and performance as component of the MPI-Earth
668 system model in different CMIP5 experimental realizations,J.Adv.Model.EarthSyst.,5, 287–315,
669 doi:10.1029/2012MS000178.
670
671 **IPCC**: Summary for Policymakers, in: IPCC Special Report on the Ocean and Cryosphere in a Changing
672 Climate, edited by: Pörtner,H.-O., Roberts, D.C., Masson-Delmotte, V., Zhai, P., Tignor, M., Poloczanska, E.,
673 Mintenbeck, K., Nicolai, M., Okem, A., Petzold, J., Rama, B., and Weyer, N., 2019.
674
675 **Ji**, Q., A. R. Babbin, A. Jayakumar, S. Oleynik, and B. B. Ward (2015), Nitrous oxide production by
676 nitrification and denitrification in the Eastern Tropical South Pacific oxygen minimum zone, Geophys. Res.
677 Lett., 42, 10,755–10,764, doi:10.1002/2015GL066853.
678
679 **Ji**, Q., Buitenhuis, E., Suntharalingam, P., Sarmiento, J. L., & Ward, B. B. (2018). Global nitrous oxide
680 production determined by oxygen sensitivity of nitrification and denitrification. Global Biogeochemical
681 Cycles, 32, 1790–1802. https://doi.org/10.1029/2018GB005887
682
683 **Kahru**, M., Leppaenen, J.-M., and Rud, O. (1993). Cyanobacterial blooms cause heating of the sea surface,
684 Mar. Ecol.-Prog. Ser., 101, 1–7.
685
686 **Kolodziejczyk**, N., W. Llovel, and E. Portela (2019). Interannual variability of upper ocean water masses as
687 inferred from Argo Array, Journal of Geophysical Research: Oceans. doi:10.1029/2018JC014866.
688
689 **Kolodziejczyk**, N., A. Prigent-Mazella and F. Gaillard (2021). ISAS temperature and salinity gridded fields.
690 SEANOE. https://doi.org/10.17882/52367
691
692 **Kortzinger**, A., Hedges, J. I., and Quay, P. D.: Redfield ratios revisited: removing the biasing effect of
693 anthropogenic CO2, Limnol. Oceanogr., 46, 964–970, 2001.
694
695 **Kwiatkowski**, L., Torres, O., Bopp, L., Aumont, O., Chamberlain, M., Christian, J. R., Dunne, J. P., Gehlen, M.,
696 Ilyina, T., John, J. G., Lenton, A., Li, H., Lovenduski, N. S., Orr, J. C., Palmieri, J., Santana-Falcón, Y.,
697 Schwinger, J., Séférian, R., Stock, C. A., Tagliabue, A., Takano, Y., Tjiputra, J., Toyama, K., Tsujino, H.,
698 Watanabe, M., Yamamoto, A., Yool, A., and Ziehn, T.: Twenty-first century ocean warming, acidification,
699 deoxygenation, and upper-ocean nutrient and primary production decline from CMIP6 model projections,
700 Biogeosciences, 17, 3439–3470, https://doi.org/10.5194/bg-17-3439-2020, 2020.
701
702 **Lam**, P., and M. Kuypers (2011). Microbial Nitrogen Cycling Processes in Oxygen Minimum Zones, Annual
703 Review of Marine Science 3:1, 317-345, doi:10.1146/annurev-marine-120709-142814
704
705 **Large**, W. G., and S. Yeager (2009). The global climatology of an interannually varying air-sea ux data set,
706 Clim. Dyn., 33, 341–364, doi:10.1007/s00382-008-0441-3.
707
708 **Lengaigne**, M., G. Madec, L. Bopp, C. Menkes, O. Aumont, and P. Cadule (2009). Bio-physical feedbacks in
709 the Arctic Ocean using an Earth system model, Geophys. Res. Lett., 36, L21602,
710 doi:10.1029/2009GL040145.
711

712 **Lengaigne**, M., Menkes, C., Aumont, O. et al. Influence of the oceanic biology on the tropical Pacific climate
713 in a coupled general circulation model. Clim. Dyn., 28**,** 503–516 (2007). https://doi.org/10.1007/s00382-
714 006-0200-2

716 **Levitus**, S., J. I. Antonov, T. P. Boyer, O. K. Baranova, H. E. Garcia, R. A. Locarnini, A.V. Mishonov, J. R.
717 Reagan, D. Seidov, E. S. Yarosh, M. M. Zweng, (2012): World Ocean heat content and thermosteric sea level
718 change (0-2000 m) 1955-2010. Geophys. Res. Lett. , 39, L10603, doi:10.1029/2012GL051106

720 **Liang**, X., Liu, C. R., Ponte, M., and Chambers, D. P. (2021). A Comparison of the Variability and Changes in
721 Global Ocean Heat Content from Multiple Objective Analysis Products During the Argo Period, J. Climate,
722 34(19), 7875–7895, https://doi.org/10.1175/JCLID-20-0794.1.

724 **Llovel**, W. and L. Terray (2016). Observed southern upper-ocean warming over 2005–2014 and associated
725 mechanisms, Environ. Res. Lett., 11, 124023.

727 **Llovel**, W., N. Kolodziejczyk, S. Close, T. Penduff, J.-M. Molines and L. Terray (2022). Imprint of intrinsic
728 ocean variability on decadal trends of regional sea level and ocean heat content using synthetic profiles,
729 Environ. Res. Lett., 17, 044063.

731 **Locarnini**, R. A., A. V. Mishonov, J. I. Antonov, T. P. Boyer, H. E. Garcia, O. K. Baranova, M. M. Zweng, C. R.
732 Paver, J. R. Reagan, D. R. Johnson, M. Hamilton, and D. Seidov, (2013). World Ocean Atlas 2013, Volume 1:
733 Temperature. S. Levitus, Ed., A. Mishonov Technical Ed.; NOAA Atlas NESDIS 73, 40 pp.

735 **Löptien**, U., C. Eden, A. Timmermann, and H. Dietze (2009), Effects of biologically induced differential
736 heating in an eddy-permitting coupled ocean-ecosystem model, J. Geophys. Res., 114, C06011,
737 doi:10.1029/2008JC004936.

738 **Lyman**, J., Good, S., Gouretski, V. et al. Robust warming of the global upper ocean. Nature **465,** 334–337
739 (2010). https://doi.org/10.1038/nature09043

740 **Madec**, G. (2008). Nemo ocean engine. Note du Pôle de modélisation de l'Institut Pierre-Simon Laplace, 27,
741 1–217.

743 **Maes**, C., and T. J. O'Kane (2014), Seasonal variations of the upper ocean salinity stratification in the
744 Tropics, J. Geophys. Res. Oceans, 119, 1706–1722, doi:10.1002/2013JC009366.

746 **Manizza**, M., C. Le Quéré, A. J. Watson, and E. T. Buitenhuis (2005), Bio-optical feedbacks among
747 phytoplankton, upper ocean physics and sea-ice in a global model, Geophys. Res. Lett., 32, L05603,
748 doi:10.1029/2004GL020778.

750 **Manizza**, M., C. Le Quéré, A. J. Watson, and E. T. Buitenhuis (2008), Ocean biogeochemical response to
751 phytoplankton-light feedback in a global model, J. Geophys. Res., 113, C10010, doi:10.1029/2007JC004478.

753 **Martinez-Rey**, J., Bopp, L., Gehlen, M., Tagliabue, A., and Gruber, N.: Projections of oceanic N_2O emissions
754 in the 21st century using the IPSL Earth system model, Biogeosciences, 12, 4133–4148,
755 https://doi.org/10.5194/bg-12-4133-2015, 2015.

757 **Marzeion**, B., Timmermann, A., Murtugudde, R., & Jin, F. (2005). Biophysical Feedbacks in the Tropical
758 Pacific, Journal of Climate, 18(1), 58-70.

760 **Meyssignac** B, Boyer T, Zhao Z, Hakuba MZ, Landerer FW, Stammer D, Köhl A, Kato S, L'Ecuyer T, Ablain M,
761 Abraham JP, Blazquez A, Cazenave A, Church JA, Cowley R, Cheng L, Domingues CM, Giglio D, Gouretski V,
762 Ishii M, Johnson GC, Killick RE, Legler D, Llovel W, Lyman J, Palmer MD, Piotrowicz S, Purkey SG, Roemmich
763 D, Roca R, Savita A, von Schuckmann K, Speich S, Stephens G, Wang G, Wijffels SE and Zilberman N (2019)

Measuring Global Ocean Heat Content to Estimate the Earth Energy Imbalance. Front. Mar. Sci. 6:432. doi: 10.3389/fmars.2019.00432

Mignot, J., D. Swingedouw, J. Deshayes, O. Marti, C. Talandier, R. Séférian, M. Lengaigne, G. Madec (2013). On the evolution of the oceanic component of the IPSL climate models from CMIP3 to CMIP5: A mean state comparison, Ocean Modelling, Volume 72, Pages 167-184, ISSN 1463-5003, https://doi.org/10.1016/j.ocemod.2013.09.001.

Morel A (1988) Optical modeling of the upper ocean in relation to its biogenous matter content (Case I waters). J Geophys Res 93:10749–10768

Morel, A. and J.-F. Berthon, 1989 : Surface pigments, algal biomass profiles, and potential production of the euphotic layer : Relationships reinvestigated in view of remote-sensing applications. Limnol. Oceanogr., 34(8), 1545–1562.

Morel A, and Maritorena S (2001) Bio-optical properties of oceanic waters: a reappraisal. J Geophys Res 106:7163–7180

Murtugudde, R., Beauchamp, J., McClain, C. R., Lewis, M., & Busalacchi, A. J. (2002). Effects of Penetrative Radiation on the Upper Tropical Ocean Circulation, Journal of Climate, 15(5), 470-486.

Myhre, G., D. Shindell, F.-M. Bréon, W. Collins, J. Fuglestvedt, J. Huang, D. Koch, J.-F. Lamarque, D. Lee, B. Mendoza, T. Nakajima, A. Robock, G. Stephens, T. Takemura and H. Zhang, (2013). Anthropogenic and Natural Radiative Forcing. In: Climate Change 2013: The Physical Science Basis. Contribution of Working Group I to the Fifth Assessment Report of the Intergovernmental Panel on Climate Change [Stocker, T.F., D. Qin, G.-K. Plattner, M. Tignor, S.K. Allen, J. Boschung, A. Nauels, Y. Xia, V. Bex and P.M. Midgley (eds.)]. Cambridge University Press, Cambridge, United Kingdom and New York, NY, USA.

Nakamoto, S., S. P. Kumar, J. M. Oberhuber, J. Ishizaka, K. Muneyama, and R. Frouin (2001), Response of the equatorial Pacific to chlorophyll pigment in a mixed layer isopycnical ocean general circulation model, Geophys. Res. Lett., 28, 2021– 2024.

Oschlies, A. (2004), Feedbacks of biotically induced radiative heating on upper-ocean heat budget, circulation, and biological production in a coupled ecosystem-circulation model, J. Geophys. Res., 109, C12031, doi:10.1029/2004JC002430.

Park, JY., Kug, JS., Seo, H. et al. Impact of bio-physical feedbacks on the tropical climate in coupled and uncoupled GCMs. Clim Dyn **43**, 1811–1827 (2014). https://doi.org/10.1007/s00382-013-2009-0

Patara, L., Vichi, M., Masina, S. et al. Global response to solar radiation absorbed by phytoplankton in a coupled climate model. Clim Dyn **39**, 1951–1968 (2012). https://doi.org/10.1007/s00382-012-1300-9

Ravishankara, A. R., J. S. Daniel, and R. W. Portmann, 2009: Nitrous oxide (N2O): The dominant ozone-depleting substance emitted in the 21st century. Science, **326**, 123–125.

Roemmich, D., and J. Gilson, 2009: The 2004–2008 mean and annual cycle of temperature, salinity, and steric height in the global ocean from the Argo Program. Prog. Oceanogr., 82, 81–100, https://doi.org/10.1016/j.pocean.2009.03.004.

Sallée, JB., Pellichero, V., Akhoudas, C. *et al.* Summertime increases in upper-ocean stratification and mixed-layer depth. Nature 591**,** 592–598 (2021). https://doi.org/10.1038/s41586-021-03303-x

Schmidtko, S., Stramma, L. & Visbeck, M. Decline in global oceanic oxygen content during the past five decades. Nature 542, 335–339 (2017).

818

819 **Séférian**, R., Berthet, S., Yool, A. et al. Tracking Improvement in Simulated Marine Biogeochemistry
820 Between CMIP5 and CMIP6. Curr Clim Change Rep **6,** 95–119 (2020). https://doi.org/10.1007/s40641-020-
821 00160-0

822

823 **Séférian**, R., Nabat, P., Michou, M., Saint-Martin, D., Voldoire, A., Colin, J., et al (2019). Evaluation of CNRM
824 Earth-System model, CNRM-ESM2-1: role of Earth system processes in present-day and future climate.
825 Journal of Advances in Modeling Earth Systems, 11. https://doi.org/10.1029/2019MS001791

826

827 **Sweeney**, C, Gnanadesikan, A., Griffies, S. M., Harrison, M. J., Rosati, A. J., & Samuels, B. L. (2005). Impacts
828 of Shortwave Penetration Depth on Large-Scale Ocean Circulation and Heat Transport, Journal of Physical
829 Oceanography, 35(6), 1103-1119.

830

831 **Takahashi**, T., Broecker, W. S., and Langer, S.: Redfield ratio based on chemical data from isopycnal
832 surfaces, J. Geophys. Res., 90, 6907–6924, 1985.

833

834 **Tian**, H., Xu, R., Canadell, J.G., R. L. Thompson, W. Winiwarter, P. Suntharalingam, E. A. Davidson, P. Ciais, R.
835 B. Jackson, G. Janssens-Maenhout, M. J. Prather, P. Regnier, N. Pan, S. Pan, G. Peters, H. Shi, F. N. Tubiello,
836 S. Zaehle, F. Zhou, A. Arneth, G. Battaglia, S. Berthet, L. Bopp, A. F. Bouwman, E. T. Buitenhuis, J. Chang,
837 Martyn P. Chipperfield, S. R.S. Dangal, E. Dlugokencky, J. Elkins, Bradley D. Eyre, B. Fu, B. Hall, A. Ito, F. Joos,
838 P. B. Krummel, A. Landolfi, G. G. Laruelle, R. Lauerwald, W. Li, S. Lienert, T. Maavara, M. MacLeod, D. B.
839 Millet, S. Olin, P. K. Patra, R. G. Prinn, P. A. Raymond, D. J. Ruiz, Guido R. van der Werf, N. Vuichard, J.
840 Wang, R. Weiss, K. C. Wells, C. Wilson, J. Yang and Y. Yao (2020). A comprehensive quantification of global
841 nitrous oxide sources and sinks. Nature 586, 248–256.
842 https://doi.org/10.1038/s41586-020-2780-0.

843

844 **Tiano**, L., E. Garcia-Robledo, T. Dalsgaard, A. H. Devol, B. B. Ward, O. Ulloa, D. E. Canfield, N. P. Revsbech
845 (2014). Oxygen distribution and aerobic respiration in the north and south eastern tropical Pacific oxygen
846 minimum zones. Deep Sea Research Part I: Oceanographic Research Papers, Volume 94, Pages 173-183,
847 https://doi.org/10.1016/j.dsr.2014.10.001.

848

849 **Timmermann**, A., and F.-F. Jin, 2002. Phytoplankton influences on tropical climate, Geophys. Res. Lett.,
850 29(23), 2104, doi:10.1029/2002GL015434.

851

852 **Tsujino**, H., Urakawa, S., Nakano, H., Small, R. J., Kim, W. M., Yeager, S. G., Danabasoglu, G., Suzuki, T.,
853 Bamber J. L., Bentsen, M., Böning, C. W., Bozec, A., Chassignet, E. P., Curchitser, E., Boeira Dias, F., Durack,
854 P. J., Griffies, S. M., Harada, Y., Ilicak, M., Josey, S. A., Kobayashi, C., Kobayashi, S., Komuro, Y., Large, W. G.,
855 Le Sommer, J., Marsland, S. J., Masina, S., Scheinert, M., Tomita, H., Valdivieso, M., and Yamazaki, D.
856 (2018). JRA-55 based surface dataset for driving ocean–sea-ice models (JRA55-do), Ocean Model., 130, 79–
857 139, https://doi.org/10.1016/j.ocemod.2018.07.002.

858

859 **Tsujino**, H., Urakawa, L. S., Griffies, S. M., Danabasoglu, G., Adcroft, A. J., Amaral, A. E., Arsouze, T., Bentsen,
860 M., Bernardello, R., Böning, C. W., Bozec, A., Chassignet, E. P., Danilov, S., Dussin, R., Exarchou, E., Fogli, P.
861 G., Fox-Kemper, B., Guo, C., Ilicak, M., Iovino, D., Kim, W. M., Koldunov, N., Lapin, V., Li, Y., Lin, P., Lindsay,
862 K., Liu, H., Long, M. C., Komuro, Y., Marsland, S. J., Masina, S., Nummelin, A., Rieck, J. K., Ruprich-Robert, Y.,
863 Scheinert, M., Sicardi, V., Sidorenko, D., Suzuki, T., Tatebe, H., Wang, Q., Yeager, S. G., and Yu, Z. (2020).
864 Evaluation of global ocean–sea-ice model simulations based on the experimental protocols of the Ocean
865 Model Intercomparison Project phase 2 (OMIP-2), Geosci. Model Dev., 13, 3643–3708,
866 https://doi.org/10.5194/gmd-13-3643-2020, 2020.

867

868 Uitz, J., Claustre, H., Morel, A., and Hooker, S. B. (2006), Vertical distribution of phytoplankton communities
869 in open ocean: An assessment based on surface chlorophyll, *J. Geophys. Res.*, 111, C08005,
870 doi:10.1029/2005JC003207.

871

872

873 **Valente**, A, Sathyendranath, S, Brotas, V, Groom, S, Grant, M, Taberner, M, Antoine, D, Arnone, R, Balch, W,
874 Barker, K, Barlow, R, Bélanger, S, Berthon, JF, Besiktepe, S, Brando, V, Canuti, E, Chavez, F, Claustre, H,
875 Crout, R, Frouin, R, Garcìa-Soto, C, Gibb, SW, Gould, R, Hooker, S, Kahru, M, Klein, H, Kratzer, S, Loisel, H,
876 McKee, D, Mitchell, BG, Moisan, T, Muller-Karger, F., O'Dowd, L, Ondrusek, M, Poulton, A, Repecaud, M,
877 Smyth, T, Sosik, HM, Twardowski, M, Voss, K, Werdell, J, Wernand, M, Zibordi, G (**2016**) A compilation of
878 global bio-optical in situ data for ocean-colour satellite applications. Earth Syst. Sci. Data, 8, 235–252, doi:
879 10.5194/essd-8-235-2016
880

881 **Wanninkhof**, R. (1992). Relationship between wind speed and gas exchange over the ocean, J. Geophys.
882 Res., 97, 7373–7382, doi:10.1029/92JC00188.
883

884 **Wanninkhof**, Rik, (2014), Relationship between wind speed and gas exchange over the ocean revisited,
885 Limnol. Oceanogr. Methods, 12, doi:10.4319/lom.2014.12.351.
886

887 **Weiss**, R. F., and B. A. Price (1980). Nitrous oxide solubility in water and seawater Marine Chemistry,
888 Volume 8, Issue 4, Pages 347-359; DOI: 10.1016/0304-4203(80)90024-9
889

890 **Wilson**, S. T., Al-Haj, A. N., Bourbonnais, A., Frey, C., Fulweiler, R. W., Kessler, J. D., Marchant, H. K., Milucka,
891 J., Ray, N. E., Suntharalingam, P., Thornton, B. F., Upstill-Goddard, R. C., Weber, T. S., Arévalo-Martínez, D.
892 L., Bange, H. W., Benway, H. M., Bianchi, D., Borges, A. V., Chang, B. X., Crill, P. M., del Valle, D. A., Farías, L.,
893 Joye, S. B., Kock, A., Labidi, J., Manning, C. C., Pohlman, J. W., Rehder, G., Sparrow, K. J., Tortell, P. D.,
894 Treude, T., Valentine, D. L., Ward, B. B., Yang, S., and Yurganov, L. N.: Ideas and perspectives: A strategic
895 assessment of methane and nitrous oxide measurements in the marine environment, Biogeosciences, 17,
896 5809–5828, https://doi.org/10.5194/bg-17-5809-2020, 2020.
897

898 **Yang**, S., B. X. Chang, M. J. Warner, T. S. Weber, A. M. Bourbonnais, A. E. Santoro, A. Kock, R. E. Sonnerup, J.
899 L. Bullister, S. T. Wilson and D. Bianchi (2020). Global reconstruction reduces the uncertainty of oceanic
900 nitrous oxide emissions and reveals a vigorous seasonal cycle, Proceedings of the National Academy of
901 Sciences, 117 (22) 11954-11960; DOI: 10.1073/pnas.1921914117
902